Energy & Environmental Science

ROYAL SOCIETY OF CHEMISTRY

PAPER

View Article Online
View Journal | View Issue

Cite this: *Energy Environ. Sci.*, 2020, **13**, 1766

Dendritic silver self-assembly in molten-carbonate membranes for efficient carbon dioxide capture†

Liam A. McNeil,‡[a] Greg A. Mutch,‡[a] Francesco Iacoviello,[b] Josh J. Bailey,[b] Georgios Triantafyllou,[a] Dragos Neagu,[a] Thomas S. Miller,[b] Evangelos I. Papaioannou,[a] Wenting Hu,[a] Dan J. L. Brett,[b] Paul R. Shearing[b] and Ian S. Metcalfe*[a]

Received 29th October 2019,
Accepted 9th March 2020

DOI: 10.1039/c9ee03497h

rsc.li/ees

Membranes for CO_2 capture should offer high permeant fluxes to keep membrane surface area small and material requirements low. Ag-supported, dual-phase, molten-carbonate membranes routinely demonstrate the highest CO_2 fluxes in this class of membrane. However, using Ag as a support incurs high cost. Here, the non-equilibrium conditions of permeation were exploited to stimulate the self-assembly of a percolating, dendritic network of Ag from the molten carbonate. Multiple membrane support geometries and Ag incorporation methods were employed, demonstrating the generality of the approach, while X-ray micro-computed tomography confirmed that CO_2 and O_2 permeation stimulated self-assembly. We report the highest flux of Ag-supported molten-salt membranes to date (1.25 ml min^{-1} cm^{-2} at 650 °C) and ultrahigh permeability (9.4×10^{-11} mol m^{-1} s^{-1} Pa^{-1}), surpassing the permeability requirement for economically-competitive post-combustion CO_2 capture, all whilst reducing the membrane-volume-normalised demand for Ag by one order of magnitude.

Broader context

CO_2 separation will likely be required for climate change mitigation and process intensification at an unprecedented scale in the future. Processes for CO_2 separation include absorption, adsorption and the use of membranes. Membranes are operated under non-equilibrium conditions, as a driving force for *e.g.* CO_2 transport is applied across the membrane. In gas separation, this driving force typically comes from a partial pressure difference between the feed and permeate sides of the membrane. Here, we exploited such non-equilibrium conditions to stimulate the self-assembly of an Ag dendritic network within a dual-phase, supported, molten-salt membrane. The percolating dendrites endowed an inert and low-cost membrane support with electronic conductivity, in turn, enhancing CO_2 permeation to a level that surpassed performance metrics required for economically-competitive CO_2 separation. The self-assembly occurred in multiple membrane geometries and using different methods of Ag incorporation, which will allow the development of a range of cost-effective and scaleable membrane fabrication routes. By exploiting the non-equilibrium conditions of permeation, typically regarded as challenging for the stability of membrane materials, we have demonstrated a new and general concept for *in situ* membrane fabrication.

Introduction

Materials and processes for CO_2 separation are widely recognised as increasingly important for climate change mitigation.[1–3] Separation of CO_2 may be facilitated by sorbents in cyclic sorption/desorption processes,[4,5] or continuously by using membrane separation.[6] Efficient membrane processes rely on high permeability membrane materials.[6,7] Dual-phase, supported, molten-salt membranes are emerging as promising next-generation devices for CO_2 separation as they remain functional at operating temperatures where other common membrane materials, *e.g.* porous inorganics and polymers, lose selectivity and stability, respectively.[3] Dual-phase membranes easily surpass the permeability-selectivity trade-off found for the majority of membranes (for polymeric membranes this is known as the Robeson upper bound),[8,9] as they offer high permeability due to liquid-like diffusivities in the molten phase, and high selectivity for CO_2 due to the chemical specificity of molten carbonate (MC). Such highly-tuned interactions between the permeant of interest and membrane material have been highlighted as one of the key design criteria for new

[a] *School of Engineering, Newcastle University, Merz Court, Newcastle Upon Tyne NE1 7RU, UK. E-mail: ian.metcalfe@newcastle.ac.uk*
[b] *Electrochemical Innovation Lab, Department of Chemical Engineering, UCL, London WC1E 7JE, UK*

† Electronic supplementary information (ESI) available. See DOI: 10.1039/c9ee03497h

‡ These authors contributed equally to this work.

efficient membranes.[6] Recent process modelling has demonstrated that dual-phase membranes outperform a commercial absorption process for pre-combustion CO_2 capture (where CO_2 must be separated from H_2). Furthermore, it has been suggested that such membranes will be competitive in post-combustion CO_2 capture from coal combustion flue gases (where the membrane feed gas contains CO_2, O_2 and N_2).[10] However, there remain a number of challenges to address, specifically, determining permeation mechanisms and increasing separation performance whilst maintaining high temperature stability.[3]

Dual-phase membranes can, in general, be categorised into two classes based on the nature of the solid support; ceramic–carbonate,[11–23] and metal–carbonate.[24–33] More recently, a combination of the two has been explored.[34–36] Ceramic–carbonate membranes are most commonly fabricated using ceramics with oxide-ion conductivity. It is proposed in the literature that ceramic–carbonate membranes exploit reversible reaction (1) at the interface between MC, ceramic support and gas phase:

$$CO_{2(g)} + O^{2-}{}_{(s)} \rightleftharpoons CO_3{}^{2-}{}_{(l)} \quad (1)$$

The forward reaction occurs at the feed side of the membrane and the reverse reaction liberates CO_2 at the permeate side.[37] Metal–carbonate membranes, where the support offers electronic conductivity, are proposed to exploit reversible reaction (2):

$$CO_{2(g)} + \frac{1}{2}O_{2(g)} + 2e^-{}_{(s)} \rightleftharpoons CO_3{}^{2-}{}_{(l)} \quad (2)$$

The presence of O_2 in the feed gas permits the forward reaction to occur at the feed side (reaction (2)), with concurrent electron and carbonate-ion transport through the membrane resulting in the release of both O_2 and CO_2 at the permeate side (reverse of reaction (2)). It is important to note that reactions (1) and (2) are unlikely to explain all observed behaviour in dual-phase membranes. For a more detailed discussion of mechanistic concerns, the reader is referred to a recent review article on this class of membrane.[38] Regardless, ceramic–carbonate membranes and metal–carbonate membranes are most applicable to pre- and post-combustion CO_2 capture, respectively, due to the requirement for O_2 in the latter case.

The first reported metal–carbonate membranes were fabricated from porous stainless-steel infiltrated with MC,[30] with CO_2 and O_2 fluxes stabilising at a level lower than that predicted by reaction (2). The authors suggested that the formation of an electronically-insulating $LiFeO_2$ layer (10^{-3} S cm^{-1}), through reaction with MC in the presence of O_2 at the feed side, lowered the electronic conductivity of the support to a value below the ionic conductivity of MC (10^0 S cm^{-1}). In this case, and if reaction (2) is sufficient to explain permeation, CO_2 and O_2 fluxes would be limited by the lower electronic conductivity of the support. To avoid these limitations, Ag-supported, metal–carbonate membranes were later investigated.[24,26,29] Ag does not form an oxide layer when in contact with MC at high temperature and offers the highest electronic conductivity of all metals (10^7 S cm^{-1}). Early Ag-supported dual-phase membranes achieved peak CO_2 and O_2 fluxes six times higher than stainless-steel membranes, 0.82 and 0.43 ml min^{-1} cm^{-2} at 650 °C, respectively, with the 2 : 1 flux ratio imposed by reaction (2) observed.[29]

While the initial performance of Ag-supported membranes is very good, it is generally not lasting (*e.g.* after ~80 hours of operation at 650 °C, CO_2 flux had decreased to ~0.70 ml min^{-1} cm^{-2}).[29] The high temperature stability issues are thought to be related to poor MC wettability on Ag, and sintering of Ag resulting in a reduction of porosity and ejection of MC.[29] Attempts have been made to address stability issues by decreasing the average pore size of the Ag support to increase capillarity,[27,33] or by coating the surface of the Ag support with a nano-layer of Al_2O_3 to improve MC wettability.[25,26,28] Alternatively, to limit Ag sintering, a refractory layer of ZrO_2 has been deposited.[31] It should also be noted that Ag is soluble in MC at the operating temperatures of dual-phase membranes,[39,40] through corrosion by MC in the presence of O_2,[41] *via* reversible reaction (3):

$$Ag^0_{(s)} \rightleftharpoons Ag^+_{(l)} + e^- \quad (3)$$

Although Ag is corroded by MC, the solubility limit of Ag^+ in MC is low (~0.05 wt%).[39,40] Reduction of Ag^+ to Ag proceeds spontaneously with the regeneration of O_2, indicating that extensive Ag corrosion could be facilitated *via* an ''oxygen cycle''.[39,40]

In this work we show how such an oxygen cycle, *i.e.* dissolution and precipitation of Ag, can be exploited advantageously to self-assemble a dendritic Ag network within low-cost Al_2O_3 dual-phase membrane supports. Self-assembly can be stimulated by the non-equilibrium conditions encountered during membrane operation, ultimately endowing inert membrane supports with electronic conductivity, and in turn, high CO_2 and O_2 fluxes. The generality of this scaleable and materials-efficient approach has been demonstrated by using multiple methods of Ag incorporation and multiple Al_2O_3 support geometries. High temperature stability relative to wholly Ag-supported membranes is shown to be greatly improved, due to retained contact between the highly wettable Al_2O_3 support and MC. Ultimately, through permeation experiments and detailed characterisation of membranes using *ex situ* X-ray micro-computed tomography, we demonstrate how self-assembling Ag dendrites in MC functionalise membranes so that they easily surpass the separation performance requirements for economically competitive CO_2 capture. This is achieved whilst lowering the membrane-volume-normalised requirement for Ag by one order of magnitude.

Results and discussion

The Al_2O_3 membrane supports used in this work were of pellet and tubular geometry, with randomly-oriented and parallel-pore networks, respectively. These were infiltrated with a ternary eutectic MC mixture (melting point, $T_m \approx 400$ °C) to form dual-phase membranes. Ag was added to the support, or MC, before infiltration, characterisation and/or permeation testing. Full procedural detail can be found in the Experimental Methods text, Fig. S1–S4 and Table S1, ESI.†

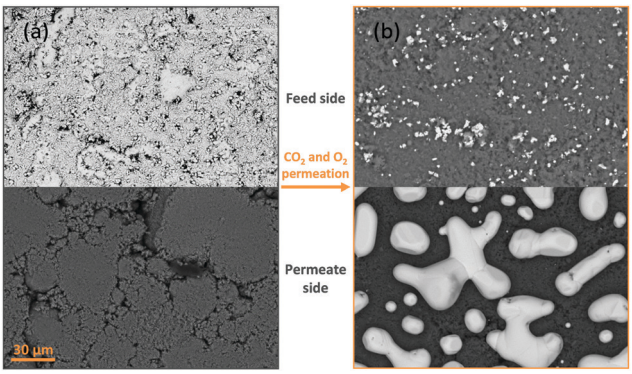

Fig. 1 SEM images of the feed and permeate sides of a Ag-plated dual-phase Al_2O_3-supported membrane before and after CO_2 and O_2 permeation. (a) An electroless-plated layer of Ag was deposited on the feed side only. (b) Following 80 hours of CO_2 and O_2 permeation at 650 °C, Ag was significantly corroded on the feed side, with ~3% appearing on the permeate side. Feed-side inlet: 50 mol% CO_2, 25 mol% O_2 and 25 mol% N_2. Permeate-side inlet: Ar.

Ag migration in dual-phase membranes

Porous pellet membrane supports were fabricated by isostatic pressing of powdered α-Al_2O_3 and an organic binder, followed by controlled sintering to form 20 mm diameter (∅) and 1.75 mm thick pellets with a randomly-oriented pore network of average pore diameter ~200 nm (Fig. S5, ESI†). In the first instance, Ag was introduced to the feed side of Al_2O_3 pellets *via* electroless plating (Fig. S1, S2 and Table S1, ESI†). After plating, the pellets had gained a 14 mm ∅, ~10 μm thick porous layer of metallic Ag (~17 mg) on the feed side, determined by SEM analysis (Fig. 1a and Fig. S6, ESI†). The permeate side of the plated membrane did not show evidence of Ag deposition, due to masking during electroless plating (Fig. 1a and Fig. S6, ESI†).

After infiltration with MC at 450 °C, during which both feed and permeate sides of the membrane were fed with a 50 mol% CO_2, 25 mol% O_2 and 25 mol% N_2 mixture to prevent carbonate decomposition, a permeation experiment was conducted at 650 °C, in a custom-made membrane permeation apparatus (Fig. S4, ESI†). The membrane feed-side inlet was kept the same (50 mol% CO_2, 25 mol% O_2 and 25 mol% N_2 mixture) with Ar fed to the permeate-side inlet, to generate a pCO_2 difference between feed and permeate sides, *i.e.* the driving force for CO_2 permeation. After 80 hours of operation a stable flux of 5.0×10^{-2} ml min^{-1} cm^{-2} was achieved, a five-fold improvement on a membrane without Ag deposition (Fig. S7, ESI†).§ SEM-EDX analysis post experiment revealed that the Ag layer on the feed-side had been corroded to a significant extent, with Ag appearing on the permeate side (Fig. 1b, 2a and Fig. S8, ESI†). SEM image analysis revealed that ~3% of the 17 mg of Ag initially deposited on the feed side had migrated to the permeate-side surface of the membrane (Fig. S9, ESI†). To determine the location and structure of the remaining ~97% of the initially-deposited Ag, *ex situ* X-ray micro-computed tomography (micro-CT) analysis was conducted to visualise the internal structure of the membrane (Fig. 2b and Experimental methods, ESI†). Ag was clearly visible on the permeate-side surface, and within the bulk of the porous pellet as a dendritic structure, confined to the central ~7 mm ∅. The location of the dendrites strongly suggested that Ag migration was driven by gas permeation, given that MC was infiltrated into the pores of the entire 20 mm ∅ Al_2O_3 pellet, the plated Ag layer was 14 mm ∅, and the active ∅ for permeation was ~7 mm due to membrane sealing (Fig. 2a and Experimental methods, ESI†). This dendritic network endowed electronic conductivity to the Al_2O_3 support, evidenced by four-point DC measurements, elaborated upon below.

Impact of Ag incorporation on CO_2 and O_2 flux

To test the generality of the approach, and reduce the complexity of the synthesis procedure, Ag was mixed as a metallic powder with the ternary eutectic carbonate powder, before infiltration into Al_2O_3 supports. This removed the requirement for Pd and hydrazine (reagents in electroless plating, ESI†), significantly reduced synthesis time, and allowed more straight-forward control of Ag quantity, all important considerations for scale-up. The Ag powder particles were larger than the average pore diameter of the Al_2O_3 pellets, so that during carbonate melting and infiltration a layer of the sparingly-soluble Ag particles was deposited on the feed-side surface. Ag mole fraction in MC was varied from 0 to 10 mol% Ag to determine the effect on stable CO_2 and O_2 fluxes at 650 °C; it was observed that CO_2 and O_2 fluxes increased with increasing Ag mole fraction (Fig. 3). At 0.25 mol% Ag, CO_2 and O_2 fluxes were 2.5×10^{-2} and 1.3×10^{-2} ml min^{-1} cm^{-2}, respectively, approximately double that of the 0 mol% Ag membrane, at 1.0×10^{-2} and 0.4×10^{-2} ml min^{-1} cm^{-2}. Within the range studied, a plateau was reached with 6 mol% Ag; fluxes of 9.5×10^{-2} and 4.8×10^{-2} ml min^{-1} cm^{-2} were achieved for CO_2 and O_2, respectively. To gain insight into CO_2 and O_2 transport an Arrhenius plot was constructed using the data from stable flux measurements from 650 to 750 °C with the 6 mol% Ag membrane (Fig. S10, ESI†). CO_2 and O_2 fluxes had apparent activation energies (E_a) of 30 kJ mol^{-1}, indicating a coupled transport mechanism.¶ E_a values were similar to a ZrO_2-coated Ag membrane (28 kJ mol^{-1}), operated at similar temperatures to the present membrane (*i.e.* >650 °C).[31] Wholly Ag-supported membranes typically fail at temperatures >650 °C, due to the sintering and wettability issues detailed above, but have E_a values of 60–80 kJ mol^{-1} at <650 °C.[25,26,29,31] Dendritic Ag membranes therefore offer improved high temperature stability, demonstrating stable fluxes at temperatures above that of wholly–Ag membranes.

In all of the above cases it is reasonable to assume that the majority of Ag was present as a solid within the membrane at

§ Throughout, we define stable flux as a minimum of 4 hours where the mean flux varied less than ±3%.

¶ In this case, the apparent activation energy corresponds to all processes that result in a transmembrane flux of CO_2 or O_2, *i.e.* surface reactions and bulk transport processes. Although technically incorrect, as the reported activation energy represents multiple processes, the values are useful for comparing our results with other membranes in the literature.

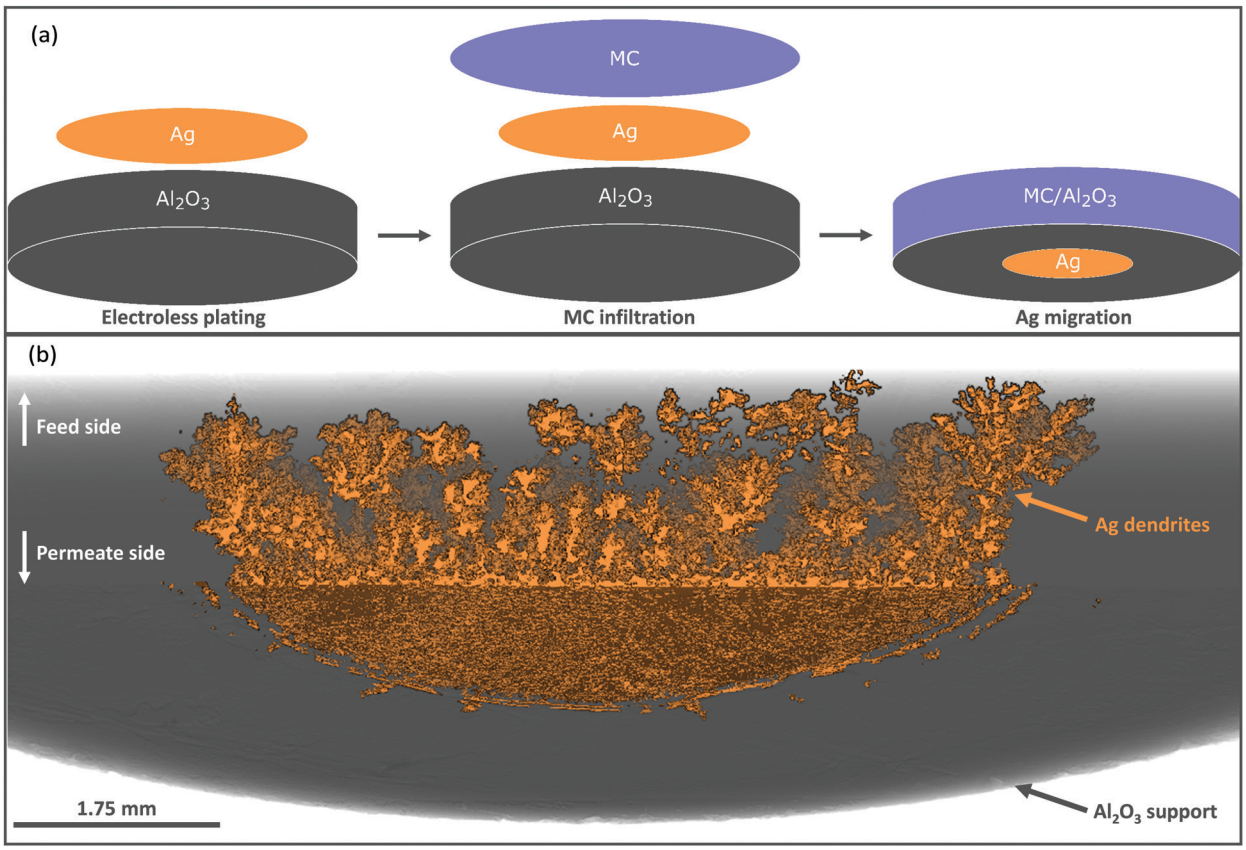

Fig. 2 Schematics and micro-CT 3D reconstruction of the cross-section of a Ag-plated dual-phase, Al_2O_3-supported membrane after CO_2 and O_2 permeation. (a) Preparation, infiltration and post-permeation schematics of pellet membranes. Following an 80 hour permeation experiment, an electroless-plated layer of Ag initially deposited on the feed side has migrated to the permeate-side surface (~3% of the initially deposited Ag). (b) The remainder of the initially-deposited Ag was found in the pellets' porosity as a dendritic Ag network throughout the central ~7 mm ∅ of the pellet, the area of the pellet available for permeation, suggesting that Ag dendrite self-assembly was stimulated by permeation. Feed-side inlet: 50 mol% CO_2, 25 mol% O_2 and 25 mol% N_2. Permeate-side inlet: Ar.

operating conditions, as the Ag loadings far exceeded the solubility limit of Ag in MC at 650 °C.[39,40] However, in all cases a small amount of Ag^+ was dissolved in MC and therefore, its effect on permeation fluxes needs to be discriminated from Ag in the solid networks. A 1.25×10^{-2} mol% Ag membrane (Ag quantity below the solubility limit of Ag^+ in MC) was prepared by dry impregnation of Ag onto the Al_2O_3 support before MC infiltration (dry impregnation was used to add such a small quantity accurately) (Fig. S11, ESI†). Dissolved Ag enhanced flux, albeit to a lesser degree than when solid Ag was present, with fluxes of 1.90×10^{-2} and 0.92×10^{-2} ml min^{-1} cm^{-2} for CO_2 and O_2, respectively (Fig. 3). Interestingly, all membranes, including the 0 and 1.25×10^{-2} mol% Ag membranes, exhibited a ~2 : 1 CO_2 : O_2 flux ratio. This suggested that the permeation mechanism in this class of membrane is more complex than that suggested by reaction (2), where an electronically-conducting support is implied as necessary for permeation to occur. It may be the case, as previously suggested in relation to an Al_2O_3-supported, molten-carbonate membrane,[22] that this was qualitative evidence for electronic conductivity in MC.[42] However, considering the present results, it is most likely that the metallic sealants employed for sealing dual-phase membranes provide transmembrane electronic conductivity. For example, visual analysis of a 0 mol% Ag membrane sealed using a silver ink showed the presence of transmembrane silver deposits and associated impact on flux during permeation experiments (Fig. S12, ESI†). Nonetheless, for our present goal, flux enhancement was most significant in the cases where Ag was present as solid dendrites, indicating that producing electronically-conductive networks is the most efficient route to achieving high transmembrane CO_2 flux.

Self-assembly of Ag dendrites

The above data clearly show that CO_2 and O_2 permeation stimulated Ag-network formation and that dual-phase membranes need not be wholly Ag-supported to exhibit the enhanced fluxes that result from permeation reliant upon electron conduction. The transient flux behaviour consistently observed at the beginning of permeation experiments, before an increase towards the high flux period defined as stable, strongly suggested that Ag dendrite growth occurred during this period.

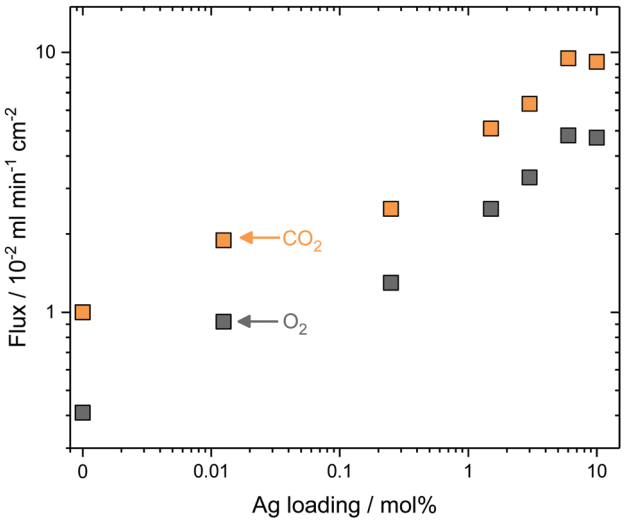

Fig. 3 Effect of Ag loading on CO_2 and O_2 fluxes at 650 °C. Stable CO_2 and O_2 fluxes (defined as a minimum of 4 hours where the mean flux varied less than ±3%) for dual-phase membranes with Ag powder loaded into molten carbonate. The standard deviation in flux during 4 hours was smaller than the data-point symbols used. Feed-side inlet: 50 mol% CO_2, 25 mol% O_2 and 25 mol% N_2. Permeate-side inlet: Ar.

To investigate Ag dendrite formation, five membranes each loaded with the 6 mol% Ag carbonate mixture previously determined as an efficient loading to realise high fluxes, were quenched at various times up to and including stable flux, for micro-CT and four-point DC analysis (Fig. 4). A further five membranes, loaded with varying amounts of Ag (0.0125–6 mol% Ag), were quenched after attaining stable flux (Fig. S13, ESI†). Regardless of the quantity of Ag in the membrane, all membranes displayed a period of low flux during the first 10 hours (Fig. 4b inset and Fig. S13, ESI†), after an initial decrease in CO_2 and O_2 mole fraction (0–5 hours) due to clearing the permeation chamber of the 50 mol% CO_2, 25 mol% O_2 and 25 mol% N_2 mixture fed to the feed- and permeate-side inlets during carbonate infiltration (Fig. 4b inset). Micro-CT was performed on membranes quenched by rapid cooling after 2, 6 and 10 hours of operation to investigate the low flux period, as well as on membranes from 20 and 120 hours, to investigate the regions of flux increase and stability (Fig. 4a and b). First, after 2 hours of permeation, Ag had already migrated from the feed-side surface to the permeate-side surface (Fig. 4a), in agreement with SEM images (Fig. 1b, Fig. S8 and S9, ESI†), and the initial micro-CT investigation (Fig. 2). After 6 hours, Ag dendrites had started to grow in the direction of the feed side from the permeate side, until they spanned the thickness of the membrane at 10 hours (Fig. 4a). Up to this point, no electronically-conductive Ag path connecting feed and permeate sides appeared to have formed, restricting fluxes to the low values observed during the first 10 hours (Fig. 4b inset). From 10 hours, the dendrites continued to grow, in both thickness and number, offering electronic conductivity across the membrane and increased flux of CO_2 and O_2 *via* reaction (2) (Fig. 4b). After 90 hours, it was likely that the majority of the initially-deposited Ag had been corroded and redistributed as dendrites within the membrane, leading to flux stabilisation (Fig. 4b). Four-point DC analysis demonstrated that membranes operated for less than 10 hours had an electrical resistance three orders of magnitude higher than membranes operated for 10 hours or more (Fig. 4c), with calculations performed on the micro-CT 3D reconstructions indicating that a substantial quantity of Ag was present within the bulk of the membrane, from 10 hours onwards, with increasing feed to permeate-side connectivity (Fig. 4d).

Ag precipitation in molten salts to form dendritic structures under an electrochemical driving force and when the molten salt is below the T_m of the metal is well-known.[43,44] In our case, self-assembly occurred due to the electrochemical gradient established within the membrane as a result of the non-equilibrium conditions of permeation. It is likely that CO_3^{2-} formation (reaction (2)) consumed electrons produced by Ag dissolution at the high pO_2 feed side (reaction (3)). CO_3^{2-} and Ag^+ ions subsequently migrated down their electrochemical potential gradient from feed to permeate side. At the permeate side, CO_3^{2-} ions decomposed to release electrons, reforming Ag from Ag^+, and releasing CO_2 and O_2 (Fig. 5). Ag first formed at the triple-phase-boundary on the low pO_2 permeate side, acting as the nucleation site for continued dendrite formation back towards the feed side. Subsequent electrons released during carbonate decomposition were transported to the tip of the growing dendrite, to recombine with Ag^+ from the melt, shortening the diffusional pathway of Ag^+, and gradually extending the Ag dendritic network until it spanned the width of the membrane. Such dendritic Ag structures have previously been used to produce electronically-conductive composites, where the unique three-dimensional fractal geometry endowed an ultra-low electrical percolation threshold.[45] Our findings demonstrate that the growth of such a dendritic network can also be used to produce self-assembling, electronically-conductive, dual-phase membranes with a substantially lower demand for Ag, elaborated upon below.

Parallel-pore Ag membranes

While micro-CT was used successfully to detail the temporal development of the dendritic network within pellet membranes (Fig. 4a), due to the voxel dimension ($\sim 10^4$ nm) being larger than the average pore diameter of the pellet supports ($\sim 10^2$ nm), the precise location and microstructure of Ag could not be accurately determined. Therefore, a tubular membrane was fabricated with 2000 single pores in a 500 μm thick closed end, where the single truncated-cone pores had a feed-side pore diameter of 150 μm and permeate-side pore diameter of 75 μm (Fig. S3, ESI†). These structures were imaged using higher resolution micro-CT, with voxel dimension $\sim 10^3$ nm, allowing the location and microstructure of Ag within single pores to be identified (Fig. 6 and Fig. S14, S15, ESI†). Again, Ag was clearly visible as a deposited layer on the permeate side (Fig. 6a and b), having migrated from the feed side during a 25-hour permeation experiment with Ag-loaded carbonates (Fig. 6c). With a reduced thickness and tortuosity compared to

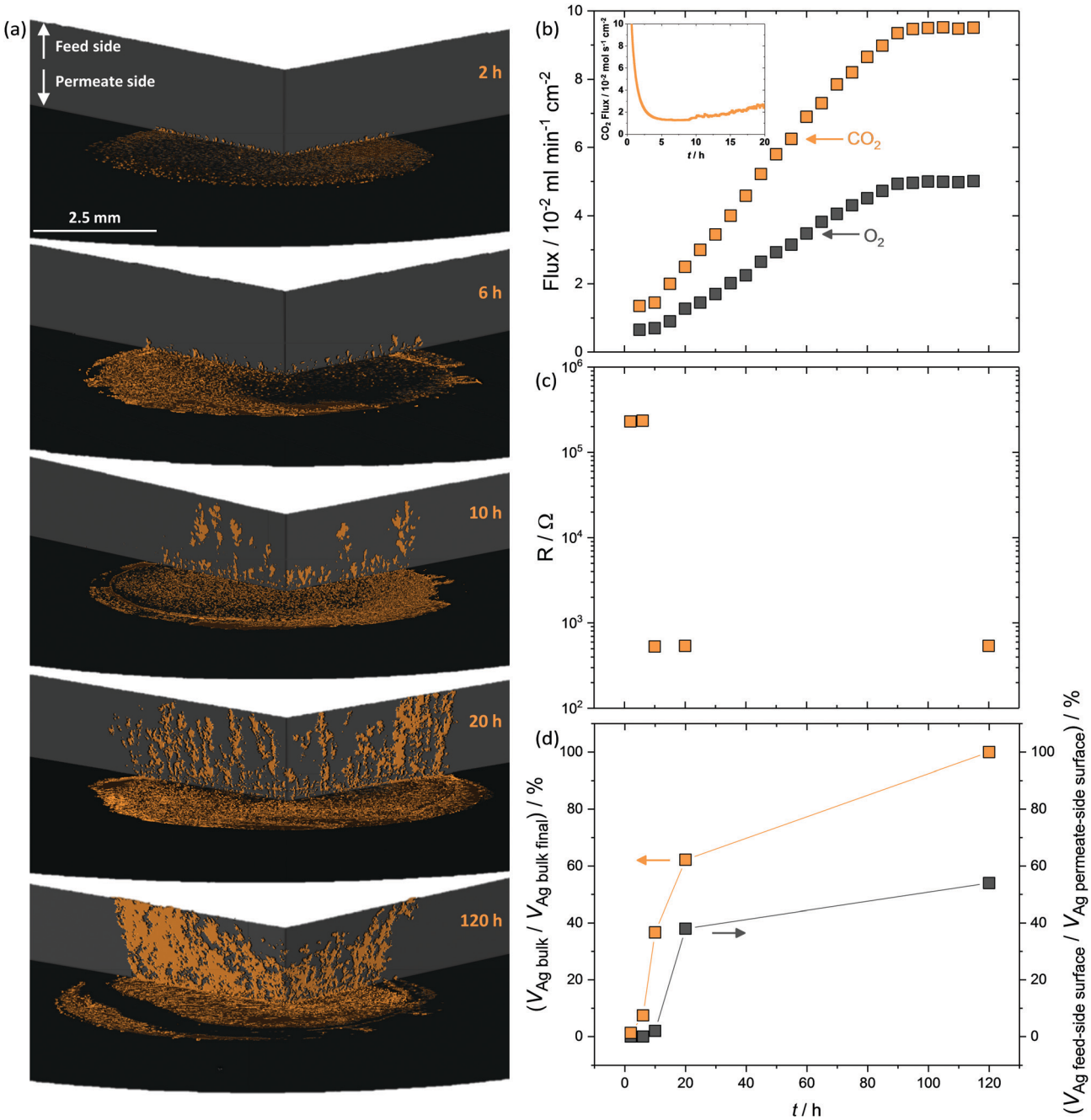

Fig. 4 Development of Ag dendrites, and membrane properties with CO_2 and O_2 flux. (a) 3D reconstructions of the cross-sections of membranes quenched at various time intervals from permeation experiments at 650 °C with 6 mol% Ag loaded pellets, (b) corresponding permeation experiment displaying typical CO_2 and O_2 fluxes with low CO_2 flux region inset, (c) four-point DC measurements of the five membranes used for 3D reconstructions, and (d) quantity of Ag in the membrane cross-section and quantity of Ag at the feed-side surface, indicating connectivity between feed and permeate side. Feed-side inlet: 50 mol% CO_2, 25 mol% O_2 and 25 mol% N_2. Permeate-side inlet: Ar.

pellet membranes, the formation of the dendritic Ag structure occurred on a shorter timescale (~10 h). Growth of dendrites from permeate to feed side was inconsistent, with Ag in selected pores failing to span the thickness of the membrane (Fig. S14, ESI†). Of course, Ag structures beneath the resolution of the micro-CT may still be present, or a small number of connected electronically-conductive networks may have provided preferential fast-transport routes, sufficient to improve overall permeation to the levels observed. However, Ag was invariably found connected to the Al_2O_3 surface, appearing to track the curvature of the single pores (Fig. 6b and Fig. S15, ESI†). It was also clear that in the majority of single pores, Ag dendrites did not cover the entirety of the pore walls. As portions of the highly wettable Al_2O_3 surface remained exposed to MC,[28] this could

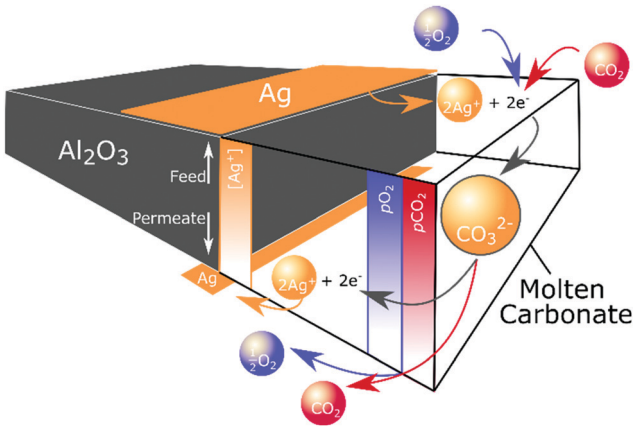

Fig. 5 Ag dendrite self-assembly. Dissolution, migration and precipitation of Ag, driven by the non-equilibrium conditions of permeation.

explain the ability of dendritic Ag membranes to operate at temperatures above which wholly-Ag membranes routinely fail (Fig. S10, ESI†).

The parallel-pore membrane also offered the opportunity to measure permeation in a low-tortuosity and reduced-thickness dendritic Ag membrane. It is known that reducing tortuosity,[46] and reducing thickness in dual-phase membranes results in higher fluxes.[14] A flux of 1.25 ml min^{-1} cm^{-2} at 650 °C was achieved (Fig. 6c), a factor of 13 higher than the pellet membranes and almost two orders of magnitude higher than a parallel-pore membrane control experiment without Ag addition (Fig. S16, ESI†). Peak fluxes for the highest flux Ag-supported membranes in the literature are typically 0.8–0.9 ml min^{-1} cm^{-2} at 650 °C,[26,29] with the ZrO_2-coated Ag membrane achieving 0.9 ml min^{-1} cm^{-2}, albeit at 850 °C,[31] and an Ag membrane with a H_2 containing sweep gas reaching

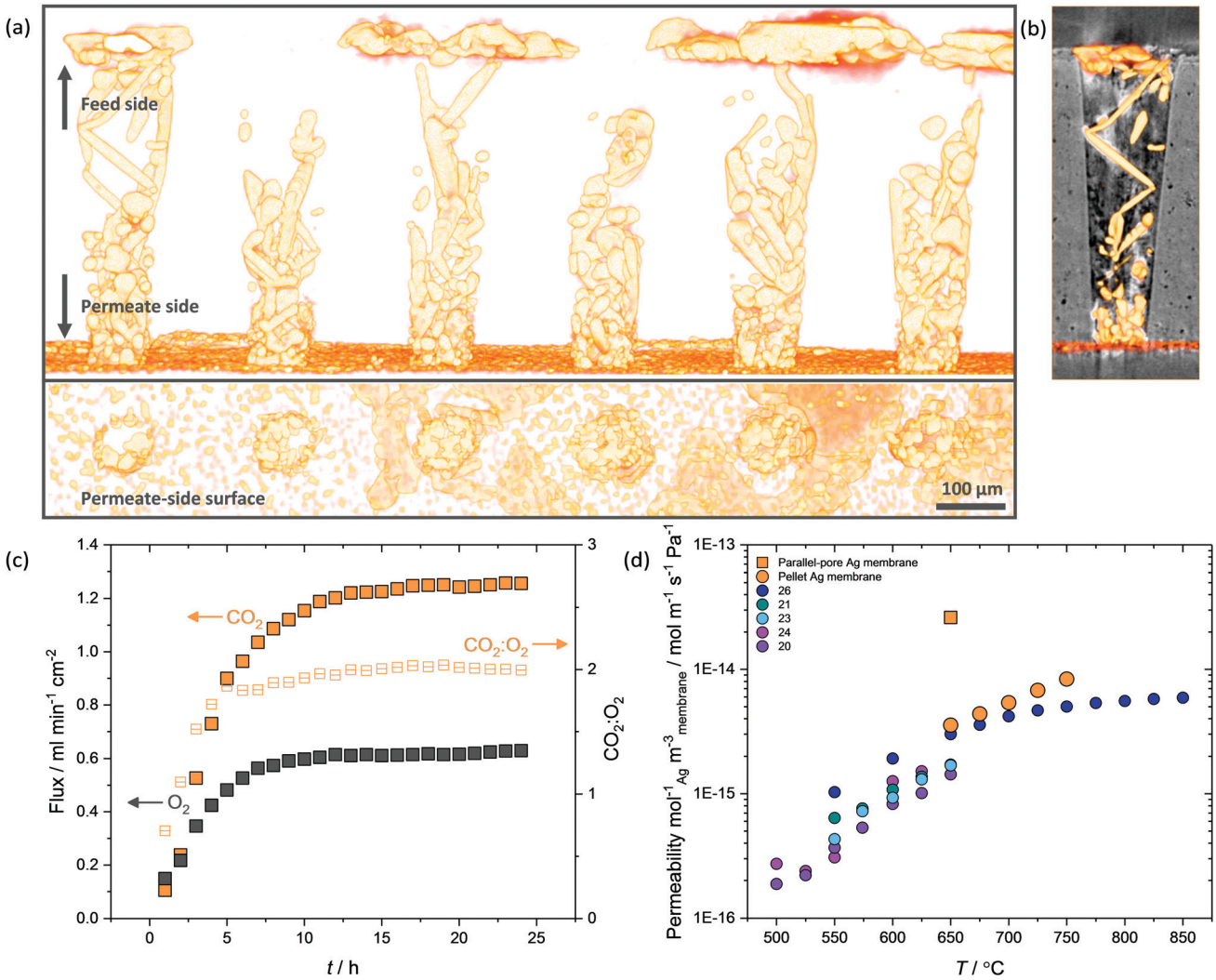

Fig. 6 Parallel-pore Ag membranes. (a) 3D reconstruction of six single pores from a parallel-pore membrane following a 25 hour permeation experiment with 6 mol% Ag loading at 650 °C (Feed-side inlet: 50 mol% CO_2, 25 mol% O_2 and 25 mol% N_2. Permeate-side inlet: Ar). A migrated Ag layer on the permeate-side surface and dendrites spanning the thickness of the membrane are visible, (b) 3D reconstruction of Ag dendrites in a single pore with Al_2O_3 pore wall, (c) CO_2 and O_2 flux evolution at 650 °C in the parallel-pore membrane and, (d) permeability of Ag membranes in the literature using CO_2 and O_2 containing feed gas, and Ar sweep gas, normalised for quantity of Ag and volume of membrane.

1.3 ml min^{-1} cm^{-2} at 700 °C.[27] ‖ Ceramic–carbonate membranes have achieved higher still CO_2 fluxes employing pre-combustion feed gases (*i.e.* containing H_2 or lacking O_2 relative to our experiments) and higher temperatures.[20,47] ‖ We note that, to the best of our knowledge, the CO_2 flux reported here at 650 °C is the highest of any ceramic- or metal-carbonate dual-phase membrane reported to date employing a post-combustion feed gas and an Ar sweep gas.[31]

Permeability, which normalises the effect of membrane thickness and the driving force for permeation (*i.e.* pCO_2 and pO_2 difference between feed and permeate sides), of parallel-pore and pellet membranes was 9.4×10^{-11} mol m^{-1} s^{-1} Pa^{-1} and 2.5×10^{-11} mol m^{-1} s^{-1} Pa^{-1}, respectively, of the same order of magnitude as Ag membranes in the literature.** However, the quantity of Ag used in our membranes was three orders of magnitude lower (*e.g.* 4 mg compared with ~4 g used in Xu *et al.*),[29] so that when permeability was normalised for the quantity of Ag used and the volume of membrane, it was clear that dendritic Ag membranes provided ultrahigh permeability at reduced cost (Fig. 6d). While it is possible that laser-drilled membrane supports will not be an economically-viable option for cost-effective scale-up, the principle of reducing the quantity of Ag is clear. A well-controlled pore forming technique such as phase inversion synthesis could be adopted to fabricate parallel-pore membranes at reduced cost, or modular membrane support geometries such as hollow fibres could be used, as Ag network growth appears to be independent of support geometry.

Recently, there has been an increasing recognition of membrane performance targets for post-combustion CO_2 capture.[48] Depending on specific mode of operation, CO_2/N_2 selectivity is targeted at 20–150 for pressure-driven operation (pressure ratio 5–15), or >140 when employing a sweep gas.[49] This selectivity must be present in membranes with CO_2 permeabilities of 10^{-13}–10^{-12} mol m^{-1} s^{-1} Pa^{-1} to be economically-competitive with existing approaches.[49,50] However, membranes generally exhibit a permeability-selectivity trade-off; for polymeric membranes, this is known as the Robeson upper bound,[9,51] and as such few membranes have surpassed these targets (Fig. 7). Dual-phase membranes offer outstanding CO_2/N_2 selectivity (>1000) as the solubility of CO_2 in molten carbonate is ~10^4 higher than N_2.[38,52] As N_2 is only detected on the permeate side of a dual-phase membrane as the result of a leak, selectivity is routinely calculated based on solubilities alone. Here, we have adopted a more conservative approach and calculated a minimum selectivity based on the limit of detection of our analytical apparatus (Experimental methods text, ESI†). Across all our permeation experiments, we thus determine a minimum CO_2/N_2 selectivity of ~100, rising to ~370 (although we note that this could be as high as >1000) (Fig. 7). Thus, our

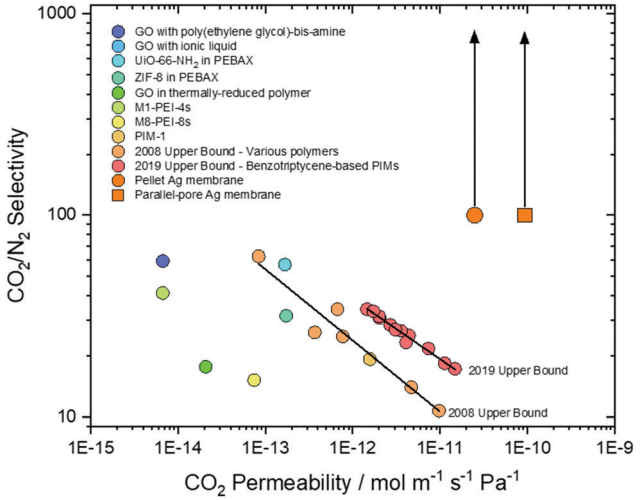

Fig. 7 State-of-the-art membrane comparison. Graphene oxide, mixed-matrix, SPONG and polymer membranes, with the 2008 and 2019 upper bounds. Pellet and parallel-pore Ag membranes are shown with minimum selectivity (~100) calculated by assuming N_2 permeation at the limit of detection of the analytical apparatus used (no N_2 was detected at the permeate-side outlet). This selectivity may be as high as >1000 if considered on the basis of CO_2/N_2 solubility.

results surpass the two most recent CO_2/N_2 Robeson upper bounds,[9,51] and a range of state-of-the-art graphene oxide,[53,54] mixed-matrix,[55–57] SPONG[48] and polymer membranes,.[9,51,58] Furthermore, dual-phase membranes are amongst a very limited range of membrane materials that can operate at >400 °C, offering exciting new separation opportunities, in *e.g.* hot flue gases without the need for gas cooling. It is also important to note that dual-phase membranes have recently been shown to self-heal autonomously at high temperature, providing confidence in their durability during operation.[59] Finally, knowledge of permeability allows one to define a membrane thickness required to achieve a target permeance (10^{-7} mol m^{-2} s^{-1} Pa^{-1} for post-combustion CO_2 capture).[60] The range of state-of-the-art membranes we have selected for comparison require thicknesses of 10^{-5}–10^{-7} m, whereas dual-phase membranes can achieve the target permeance at 10^{-4} m thickness. For this reason, the membranes we report here (~500 μm) are approaching the permeance required for economically-competitive post-combustion CO_2 capture, without the need for extreme membrane thinning and the associated costs.

Conclusions

We have prepared dual-phase, supported, molten-salt membranes which exploit self-assembling electronically-conductive dendritic Ag networks. Pellet and tubular membranes, made from low-cost Al_2O_3, with a range of methods for Ag incorporation were used, demonstrating generality. Through permeation-driven non-equilibrium growth of Ag dendrites, from small quantities of added Ag, low-cost, low-flux membrane materials were transformed into low-cost, high-flux membranes. These membranes achieved the permeance required for cost-effective CO_2 capture

‖ We note that reported fluxes are often the highest flux achieved during the first ~10–20 hours of a permeation experiment, with stable fluxes at ~80 hours some ~10% lower than the values highlighted here.

** Note that we do not account for the driving force of O_2 in our calculation of permeability (and therefore permeance) as this is the procedure widely adopted with Ag-supported membranes, thus allowing us to compare.

from post-combustion gas streams (10^{-7} mol m^{-2} s^{-1} Pa^{-1}).[60] We reported the highest flux of any metal–carbonate, dual-phase membrane to date (1.25 ml min^{-1} cm^{-2} at 650 °C), and ultrahigh permeabilities (10^{-11} mol m^{-1} s^{-1} Pa^{-1}), outperforming the permeability requirement for economically-competitive CO_2 capture (10^{-13}–10^{-12} mol m^{-1} s^{-1} Pa^{-1}).[49,50] We suggest that non-equilibrium growth of dendritic Ag networks in MC could be employed as a cost-effective strategy to prepare high performance CO_2-permeable membranes, with improved high temperature stability. More generally, we propose that the non-equilibrium conditions of membrane permeation, routinely considered as deleterious for long-term stability, can instead be considered as favourable conditions to add advantageous functionality to membranes *in situ*.

Conflicts of interest

There are no conflicts to declare.

Acknowledgements

The authors wish to thank Dr Oliver B. Camus at Bath University for conducting mercury intrusion porosimetry measurements and Dr Maggie White at Newcastle University for conducting X-ray diffraction analyses. The research leading to these results has received funding from the European Research Council under the European Union's Seventh Framework Programme (FP/2007-2013)/ERC Grant Agreement Number 320725 and from the Engineering & Physical Sciences Research Council (EPSRC) *via* grants EP/M01486X/1, EP/P007767/1 and EP/P009050/1. X-ray access was supported by UCL and EPSRC under EP/M028100/1. L. A. M. would like to thank the Newcastle University EPSRC DTP. G. A. M. would like to thank the EPSRC for his Doctoral Prize Fellowship (EP/M50791X/1) and Newcastle University for a Newcastle University Academic Track (NUAcT) Fellowship. T. S. M. would like to thank the EPSRC for his Fellowship (EP/P023851/1). P. R. S. acknowledges the support of the Royal Academy of Engineering (CIET 1718/59). Data supporting this publication is available under a Creative Commons Attribution 4.0 International license, see DOI: 10.25405/data.ncl.9608369.

Notes and references

1 N. MacDowell, N. Florin, A. Buchard, J. Hallett, A. Galindo, G. Jackson, C. S. Adjiman, C. K. Williams, N. Shah and P. Fennell, *Energy Environ. Sci.*, 2010, **3**, 1645.
2 M. E. Boot-Handford, J. C. Abanades, E. J. Anthony, M. J. Blunt, S. Brandani, N. Mac Dowell, J. R. Fernández, M.-C. Ferrari, R. Gross, J. P. Hallett, R. S. Haszeldine, P. Heptonstall, A. Lyngfelt, Z. Makuch, E. Mangano, R. T. J. Porter, M. Pourkashanian, G. T. Rochelle, N. Shah, J. G. Yao and P. S. Fennell, *Energy Environ. Sci.*, 2014, **7**, 130.
3 M. Bui, C. S. Adjiman, A. Bardow, E. J. Anthony, A. Boston, S. Brown, P. S. Fennell, S. Fuss, A. Galindo, L. A. Hackett, H. J. Herzog, G. Jackson, J. Kemper, S. Krevor, G. C. Maitland, M. Matuszewski, I. S. Metcalfe, C. Petit, G. Puxty, J. Reimer, D. M. Reiner, E. S. Rubin, S. A. Scott, N. Shah, B. Smit, J. P. M. Trusler, P. Webley, J. Wilcox and N. MacDowell, *Energy Environ. Sci.*, 2018, **11**, 1062–1176.
4 G. T. Rochelle, *Science*, 2009, **325**, 1652–1654.
5 J. Blamey, E. J. Anthony, J. Wang and P. S. Fennell, *Prog. Energy Combust. Sci.*, 2010, **36**, 260–279.
6 H. B. Park, J. Kamcev, L. M. Robeson, M. Elimelech and B. D. Freeman, *Science*, 2017, **356**, 1138–1148.
7 S. Wang, X. Li, H. Wu, Z. Tian, Q. Xin, G. He, D. Peng, S. Chen, Y. Yin, Z. Jiang and M. D. Guiver, *Energy Environ. Sci.*, 2016, **9**, 1863–1890.
8 L. M. Robeson, *J. Membr. Sci.*, 1991, **62**, 165–185.
9 L. M. Robeson, *J. Membr. Sci.*, 2008, **320**, 390–400.
10 R. Anantharaman, T. Peters, W. Xing and M. Fontaine, *Faraday Discuss.*, 2016, **192**, 251–269.
11 X. Dong, J. Ortiz Landeros and Y. S. Lin, *Chem. Commun.*, 2013, **49**, 9654–9656.
12 Z. Rui, M. Anderson, Y. Li and Y. S. Lin, *J. Membr. Sci.*, 2012, **417–418**, 174–182.
13 T. T. Norton and Y. S. Lin, *Solid State Ionics*, 2014, **263**, 172–179.
14 M. Anderson and Y. S. Lin, *J. Membr. Sci.*, 2010, **357**, 122–129.
15 H. Ahn, D. Kim, V. M. A. Melgar, J. Kim, M. R. Othman, H. V. P. Nguyen, J. Han and S. P. Yoon, *J. Ind. Eng. Chem.*, 2014, **20**, 6–11.
16 O. Ovalle-Encinia, H. Pfeiffer and J. Ortiz-Landeros, *J. Membr. Sci.*, 2018, **547**, 11–18.
17 T. T. Norton, B. Lu and Y. S. Lin, *J. Membr. Sci.*, 2014, **467**, 244–252.
18 M. Zuo, S. Zhuang, X. Tan, B. Meng, N. Yang and S. Liu, *J. Membr. Sci.*, 2014, **458**, 58–65.
19 J. Tong, L. Zhang, M. Han and K. Huang, *J. Membr. Sci.*, 2015, **477**, 1–6.
20 L. Zhang, N. Xu, X. Li, S. Wang, K. Huang, W. H. Harris and W. K. S. Chiu, *Energy Environ. Sci.*, 2012, **5**, 8310–8317.
21 L. Zhang, X. Li, S. Wang, K. G. Romito and K. Huang, *Electrochem. Commun.*, 2011, **13**, 554–557.
22 J. L. Wade, C. Lee, A. C. West and K. S. Lackner, *J. Membr. Sci.*, 2011, **369**, 20–29.
23 T. T. Norton, J. Ortiz-Landeros and Y. S. Lin, *Ind. Eng. Chem. Res.*, 2014, **53**, 2432–2440.
24 L. Zhang, Y. Gong, K. S. Brinkman, T. Wei, S. Wang and K. Huang, *J. Membr. Sci.*, 2014, **455**, 162–167.
25 L. Zhang, Y. Gong, J. Yaggie, S. Wang, K. Romito and K. Huang, *J. Membr. Sci.*, 2014, **453**, 36–41.
26 J. J. Tong, X. L. Lei, J. Fang, M. F. Han and K. Huang, *J. Mater. Chem. A*, 2016, **4**, 1828–1837.
27 J. Fang, J. Tong and K. Huang, *J. Membr. Sci.*, 2016, **505**, 225–230.
28 J. Tong, F. Si, L. Zhang and J. Fang, *Chem. Commun.*, 2015, **51**, 2936–2938.
29 N. Xu, X. Li, M. A. Franks, H. Zhao and K. Huang, *J. Membr. Sci.*, 2012, **401–402**, 190–194.
30 S. J. Chung, J. H. Park, D. Li, J. I. Ida, I. Kumakiri and J. Y. S. Lin, *Ind. Eng. Chem. Res.*, 2005, **44**, 7999–8006.

31 P. Zhang, J. Tong, Y. Jee and K. Huang, *Chem. Commun.*, 2016, **52**, 9817–9820.
32 L. Zhang, J. Tong, Y. Gong, M. Han, S. Wang and K. Huang, *J. Membr. Sci.*, 2014, **468**, 373–379.
33 J. Fang, N. Xu, T. Yang, P. Zhang, J. Tong and K. Huang, *J. Membr. Sci.*, 2017, **523**, 439–445.
34 P. Zhang, J. Tong and K. Huang, *ACS Sustainable Chem. Eng.*, 2018, **6**, 14162–14169.
35 P. Zhang, J. Tong and K. Huang, *J. Mater. Chem. A*, 2017, **5**, 12769–12773.
36 O. Ovalle-Encinia, H. Pfeiffer and J. Ortiz-Landeros, *Ind. Eng. Chem. Res.*, 2018, **57**, 9261–9268.
37 Z. Rui, M. Anderson, Y. S. Lin and Y. Li, *J. Membr. Sci.*, 2009, **345**, 110–118.
38 G. A. Mutch, L. Qu, G. Triantafyllou, W. Xing, M.-L. Fontaine and I. S. Metcalfe, *J. Mater. Chem. A*, 2019, **7**, 12951–12973.
39 G. J. Janz, A. Conte and E. Neuenschwander, *Corrosion*, 1963, **19**, 292–294.
40 G. J. Janz, E. Neuenschwander and A. Conte, *Corros. Sci.*, 1963, **3**, 177–180.
41 J. M. Fisher and P. S. Bennett, *J. Mater. Sci.*, 1991, **26**, 749–755.
42 H. Nafe, *ECS J. Solid State Sci. Technol.*, 2014, **3**, 23–29.
43 T. B. Reddy, *J. Electrochem. Soc.*, 1966, **113**, 117–123.
44 A. M. S. El Din and G. Wranglén, *Electrochim. Acta*, 1962, **7**, 79–90.
45 C. Yang, X. Cui, Z. Zhang, S. W. Chiang, W. Lin, H. Duan, J. Li, F. Kang and C. P. Wong, *Nat. Commun.*, 2015, **6**, 1–10.
46 J. Ortiz-Landeros, T. Norton and Y. S. Lin, *Chem. Eng. Sci.*, 2013, **104**, 891–898.
47 X. Dong, H. C. Wu and Y. S. Lin, *J. Membr. Sci.*, 2018, **564**, 73–81.
48 G. He, S. Huang, L. F. Villalobos, J. Zhao, M. Mensi, E. Oveisi, M. Rezaei and K. V. Agrawal, *Energy Environ. Sci.*, 2019, **12**, 3305–3312.
49 K. Ramasubramanian, H. Verweij and W. S. Winston Ho, *J. Membr. Sci.*, 2012, **421–422**, 299–310.
50 N. Bryan, E. Lasseuguette, M. Van Dalen, N. Permogorov, A. Amieiro, S. Brandani and M. C. Ferrari, *Energy Procedia*, 2014, **63**, 160–166.
51 B. Comesana-Gandara, J. Chen, C. G. Bezzu, M. Carta, I. Rose, M.-C. Ferrari, E. Esposito, A. Fuoco, N. B. McKeown and J. C. Jansen, *Energy Environ. Sci.*, 2019, **12**, 2733–2740.
52 M. R. Cerón, L. S. Lai, A. Amiri, M. Monte, S. Katta, J. C. Kelly, M. A. Worsley, M. D. Merrill, S. Kim and P. G. Campbell, *J. Membr. Sci.*, 2018, **567**, 191–198.
53 S. Wang, Y. Xie, G. He, Q. Xin, J. Zhang, L. Yang, Y. Li, H. Wu, Y. Zhang, M. D. Guiver and Z. Jiang, *Angew. Chem., Int. Ed.*, 2017, **56**, 14246–14251.
54 M. Karunakaran, L. F. Villalobos, M. Kumar, R. Shevate, F. H. Akhtar and K. V. Peinemann, *J. Mater. Chem. A*, 2017, **5**, 649–656.
55 P. D. Sutrisna, J. Hou, M. Y. Zulkifli, H. Li, Y. Zhang, W. Liang, D. M. D'Alessandro and V. Chen, *J. Mater. Chem. A*, 2018, **6**, 918–931.
56 P. D. Sutrisna, J. Hou, H. Li, Y. Zhang and V. Chen, *J. Membr. Sci.*, 2017, **524**, 266–279.
57 S. Kim, J. Hou, Y. Wang, R. Ou, G. P. Simon, J. G. Seong, Y. M. Lee and H. Wang, *J. Mater. Chem. A*, 2018, **6**, 7668–7674.
58 A. K. Sekizkardes, V. A. Kusuma, G. Dahe, E. A. Roth, L. J. Hill, A. Marti, M. Macala, S. R. Venna and D. Hopkinson, *Chem. Commun.*, 2016, **52**, 11768–11771.
59 M. Kazakli, G. A. Mutch, L. Qu, G. Triantafyllou and I. S. Metcalfe, *J. Membr. Sci.*, 2020, **600**, 117855.
60 T. C. Merkel, H. Lin, X. Wei and R. Baker, *J. Membr. Sci.*, 2010, **359**, 126–139.